J. Fluid Mech. (1974), *vol.* 65, *part* 4, *pp.* 657–688
Printed in Great Britain

Dynamics of establishment of selective withdrawal of a stratified fluid from a line sink. Part 1. Theory

By HSIEN-PING PAO AND TIMOTHY W. KAO

Department of Aerospace and Atmospheric Sciences,
The Catholic University of America, Washington, D.C. 20017

(Received 30 August 1973 and in revised form 4 March 1974)

An investigation is made of selective withdrawal of a linear stratified fluid from a line sink in a channel of depth d. The flow is characterized by a densimetric Froude number $F = Q/Nd^2$, where Q is the discharge per unit width and N is the Väisälä frequency. The dynamics of establishment of flow are investigated theoretically. Analytic results are obtained from a linearized theory based on a systematic perturbation scheme for small values of F. These results lead to a proper identification of the successive arrival of 'columnar disturbance modes' as the mechanism responsible for the development of flow concentration in the withdrawal region. Viscous and diffusive effects are also examined. For larger times and higher discharges (higher values of F), nonlinear effects become important, and the full Navier–Stokes equations are now solved numerically by a finite-difference procedure in a 'stretched' co-ordinate system. The solutions indicate that the establishment of the steady flow field is due to the successive arrival and interaction of 'columnar disturbance modes'. Steady-state solutions are also presented, and a similarity profile is obtained. Comparison of the theoretical findings with experimental results are presented in part 2. Agreement with experimental measurements is found to be excellent.

1. Introduction

The main characteristic that distinguishes a stratified medium in a gravitational field from a homogeneous medium is its ability to sustain internal gravity waves and flow concentrations. This has been observed in nature, it has widespread geophysical implications, and it is of fundamental importance for fluid mechanics. That this is so for water quality management is shown by the 'selective withdrawal' of water in a reservoir (Wunderlich & Elder 1971; Wunderlich 1971). In deep lakes or reservoirs, seasonal change in solar radiation is the cause of density stratification from spring to late autumn. Solar heating, aided by mixing due to surface winds, penetrates downward, to establish a warm upper layer (the *epilimnion*), followed by a transition layer (the *metalimnion* or *thermocline*), which leads to the lower dense cold region (the *hypolimnion*). In north temperate lakes (such as Cayuga lake in upper New York state), the hypolimnion is thick, whereas, in more southern lakes or reservoirs (such as those in the Tennessee Valley Authority (TVA) river basin system), the metalimnion is thick and shows

an almost linear increase in density with depth. When outflow is withdrawn from density-stratified reservoirs, the water comes mainly from zones at elevations corresponding approximately, in hydroelectric dams, to the level of the intake openings leading to the turbine penstocks. This is *selective withdrawal*. The various water quality parameters (such as temperature, dissolved oxygen (DO), foreign mineral contents, etc.) are interrelated with the density and advected by the withdrawal current. Thus, selective withdrawal has a long-range effect on the environment, especially on the quality of drinking water and on aquatic life, in both the reservoir and its downstream river (Wunderlich & Elder 1968). It has been reported (*Sport Fishing U.S.A.*, 1971, Government Printing Press) that the population of some warm-water species declines drastically after a dam begins to release cold water from the lower layers of its reservoir. Furthermore, when a hydroelectric power plant operates as a peaking plant, the quality and quantity of discharge in the downstream river also undergo periodic variation.

In the present study, selective withdrawal from a line sink is investigated in terms of the dynamics of establishment. In part 1 we present analytic results from a linearized theory, and numerical solutions of the full nonlinear governing equations. In part 2 (Kao, Pao & Wei 1974) we make comparisons between experimental data and the relevant theoretical, numerical and field results. The emphasis is on the nature of the propagation of disturbances, the development of the flow field, and the final steady-state velocity field.

The analysis of the flow of a linearly stratified fluid into a horizontal line sink was first made by Yih (1958), who obtained the exact steady-state solution, valid for $\pi^{-1} < F < \infty$, where F is the densimetric Froude number Q/Nd^2 (Q is the discharge rate per unit width, d is the depth of the channel, the Väisälä frequency $N = (\kappa g)^{\frac{1}{2}}$, and $\kappa = -(1/\rho_0)d\bar{\rho}/dZ$ is the slope of the density variation far upstream, a constant). Yih assumed the velocity and density to be undisturbed far upstream, so that no solution was obtained for $F < \pi^{-1}$. Debler (1959) then showed by experiment that $F \sim \pi^{-1}$ is indeed a critical Froude number, above which Yih's solution is valid, and below which the flow separates into a flowing region near the level of the sink, the fluid remaining essentially stagnant elsewhere (i.e. selective withdrawal occurs).† Debler also found that the densimetric Froude number F_1, based upon the depth of the flowing zone, remained essentially constant, having a value of 0·28 for various discharges. By introducing a free streamline which separates the flowing zone from the completely stagnant regime, Kao (1965, 1970) obtained a family of solutions corresponding to $\pi^{-1} < F_1 < \infty$ for any given discharge rate. Kao (1970) gave $F_1 = 0{\cdot}33$ as the unique Froude number for all separated flows. In his solution, the thickness of the flow zone remains constant with distance upstream, as a consequence of the inviscid assumption. Koh (1966*a*) obtained a steady-state solution for an infinite medium, incorporating viscous and diffusive effects and neglecting the nonlinear terms. His solution predicts that the growth rate of the thickness of the flowing zone is proportional to $X^{\frac{1}{3}}$, where X is distance from the sink. By partitioning the flow

† The analogous phenomenon of selective withdrawal in rotating fluids was studied by Pao & Kao (1969), Shih & Pao (1971) and Pao & Shih (1973).

into inner and outer regimes, and using the outer flow as the upstream boundary condition for his inner flow equations, Imberger (1972) obtained a steady-state solution, which improved Koh's prediction about the thickness of the flowing zone, by requiring that the flowing zone be thick enough to achieve Kao's value near to the sink. These studies were all concerned with the steady-state problem, so that the dynamics of establishment were not investigated. Trustrum (1964) solved a linearized initial-value problem based on the Boussinesq and Oseen approximations, and obtained an asymptotic solution for large times, valid for $F > \pi^{-1}$. The approximations involved, however, invalidated her solutions for $F < \pi^{-1}$. Koh (1966*b*) also solved a linearized initial-value problem for a sink in an infinite medium. His solution predicted an increase in the horizontal velocity towards the sink with time along the horizontal plane containing the line sink. But this increase is felt instantaneously at all distances away from the sink, by an amount inversely proportional to the radial distance from the sink, which is physically unrealistic. The time-dependent behaviour of stratified flow into a line sink is therefore largely unexplored. To trace the actual history of flow establishment, an initial-value problem is solved, and solutions obtained for various times. For low values of F, a linearized inviscid problem, obtained by a systematic perturbation scheme, is solved analytically. Viscous and diffusive effects are also examined. For larger F, nonlinear interactions become important, and the full Navier–Stokes equations are solved numerically. The solutions indicate that the establishment of the steady flow field is due to the successive arrival and interaction of columnar disturbance modes. Steady-state numerical solutions are also found. A similarity velocity profile is obtained.

2. The linearized initial-value problem

2.1. *Formulation of problem and linearized solution for velocity field*

We consider the flow into a line sink situated at the origin of an X, Z co-ordinate system in a channel of depth d (as shown in figure 1). The initial-value problem corresponds to starting the discharge suddenly from an initially stationary state which is stratified linearly. We seek a consistent perturbation scheme valid for finite times. If Q is the discharge per unit width of the channel, then, with d taken as the characteristic length, the characteristic velocity is U with $U = Q/d$. Thus, we write $(X, Z) = (xd, zd)$, and the corresponding velocities

$$(u^*, w^*) = (uU, wU),$$

so that (x, z) and (u, w) are dimensionless. If $\bar{\rho}(Z)$ is the initial stratification and $\bar{\rho}(0) \equiv \rho_0$, $\bar{\rho}(d) \equiv \rho_s$, then $N^{-1} = (\kappa g)^{-\frac{1}{2}}$ gives the proper characteristic time.

We let the time-dependent density field ρ^* be equal to $\rho_0(1-\kappa Z)+\rho'$. Cross-differentiating Euler's equations of motion, and using continuity, we have, after normalization with the above characteristic quantities, the vorticity equation

$$\frac{\partial \zeta}{\partial t} + F\left(u\frac{\partial \zeta}{\partial x} + w\frac{\partial \zeta}{\partial z}\right) = \frac{\partial \rho}{\partial x}, \tag{1}$$

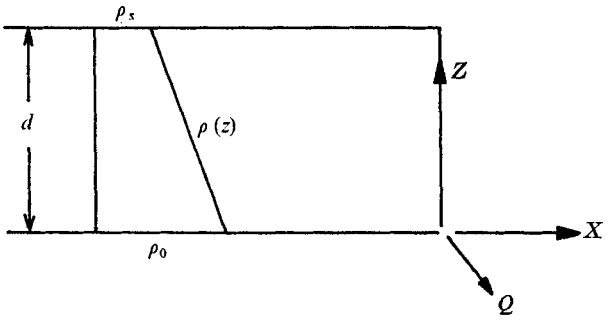

FIGURE 1. Definition sketch.

where $\rho = \rho'/(\rho_0 NQ/gd)$, ζ is the dimensionless vorticity, t the dimensionless time. As usual, gravity is acting in the negative z direction. The equation of density conservation upon normalization is

$$\frac{\partial \rho}{\partial t} + F\left(u\frac{\partial \rho}{\partial x} + w\frac{\partial \rho}{\partial z}\right) = w. \tag{2}$$

From continuity we have $u = \partial\Psi/\partial z$, $w = -\partial\Psi/\partial x$, so that

$$\zeta \equiv \left(\frac{\partial u}{\partial z} - \frac{\partial w}{\partial x}\right) = \left(\frac{\partial^2}{\partial x^2} + \frac{\partial^2}{\partial z^2}\right)\Psi \equiv \nabla^2\Psi.$$

On substitution of these relations into (1) and (2), we have

$$\frac{\partial}{\partial t}\nabla^2\Psi + F\frac{\partial(\nabla^2\Psi, \Psi)}{\partial(x, z)} = \frac{\partial \rho}{\partial x}, \tag{3}$$

$$\frac{\partial}{\partial t}\rho + F\frac{\partial(\rho, \Psi)}{\partial(x, z)} = -\frac{\partial \Psi}{\partial x}. \tag{4}$$

We now introduce a perturbation series in F,

$$\Psi = \psi^0 + F\psi_1 + F^2\psi_2 + \ldots,$$
$$\rho = \rho^0 + F\rho_1 + F^2\rho_2 + \ldots.$$

The zeroth-order equations are then the well-known linearized equations

$$\frac{\partial}{\partial t}\nabla^2\psi^0 = \frac{\partial \rho^0}{\partial x}, \quad \frac{\partial}{\partial t}\rho^0 = -\frac{\partial \psi^0}{\partial x}. \tag{5), (6}$$

These are to be solved subject to the boundary conditions $\psi^0 = 0$ for $z = 0$, $x < 0$; $\psi^0 = H(t)$ for $z = 1$, $x < 0$, and for $0 < z \leqslant 1$, $x = 0$; and the initial condition $u = w = 0$ and $\rho = 0$. ($H(t)$ is the Heaviside unit step function.)

We cast the problem into a slightly more convenient form by letting

$$\psi = \psi^0 - zH(t).$$

On eliminating ρ^0 from (5) and (6), the initial/boundary-value problem in ψ is

$$\frac{\partial^2}{\partial t^2}(\nabla^2\psi) + \frac{\partial^2 \psi}{\partial x^2} = 0 \quad (x < 0, \quad 0 < z < 1, \quad t \geqslant 0), \tag{7}$$

(i) $\psi = 0$ for $z = 0$, $x < 0$,

(ii) $\psi = 0$ for $z = 1$, $x < 0$,

(iii) $\psi = (1-z)H(t)$ for $0 < z \leqslant 1$, $x = 0$,

(iv) $|\psi| < \infty$ for $0 \leqslant z \leqslant 1$, $x = -\infty$,

and (v) $\dfrac{\partial}{\partial t}\nabla^2\psi = 0$, $\nabla^2\psi = 0$ at $t = 0$.

We introduce the Laplace transform in t and its inverse, and set

$$\overline{\psi}(x,z,s) = \int_0^\infty \psi(x,z,t)\exp\{-st\}\,dt,$$

$$\psi(x,z,t) = \int_{\gamma-i\infty}^{\gamma+i\infty} \frac{1}{2\pi i}\overline{\psi}(x,z,s)\exp\{st\}\,ds,$$

where γ is a real number that places the path of integration to the right of all singularities of the integrand in the complex s plane. On taking the Laplace transform of (7), and solving the resulting boundary-value problem by separation of variables, we get, after some calculation, the solution†

$$\overline{\psi}(x,z,s) = \sum_{n=1}^{\infty} a_n(s)\exp\left\{\frac{n\pi s x}{(1+s^2)^{\frac{1}{2}}}\right\}\sin n\pi z, \quad a_n = \frac{2}{n\pi s}. \tag{8}$$

From (8) we see immediately, on invoking the Tauberian theorem for $t \to 0$, that, as $s \to \infty$,

$$\lim_{s\to\infty} s.\overline{\psi} = \sum_{n=1}^{\infty}\frac{2}{n\pi}\exp(n\pi x)\sin n\pi z, \quad x < 0,$$

or

$$\psi^0(x,z,0) = z + \sum_{n=1}^{\infty}\frac{2}{n\pi}\exp(n\pi x)\sin n\pi z, \quad x < 0, \tag{9}$$

which is the solution for a potential flow into a line sink as it should be.

For $t \neq 0$,

$$\psi^0(x,z,t) = z + \sum_{n=1}^{\infty}\frac{2}{n\pi}\sin n\pi z\left[\frac{1}{2\pi i}\int_{\gamma-i\infty}^{\gamma+i\infty}\frac{1}{s}\exp\left\{\frac{n\pi s x}{(1+s^2)^{\frac{1}{2}}} + st\right\}ds\right]. \tag{10}$$

The integral in (10) is now to be evaluated in the complex s plane. It is observed that the integral has branch points at $s = \pm i$ and a simple pole at $s = 0$. The path of integration Γ_1 is indicated in figure 2. This integration may be most readily performed by deforming the contour around the Riemann sphere, and evaluating it around a circle Γ_2 about the north pole by the transformation $\eta = s^{-1}$. Thus we can write the integral in (10) as

$$\oint_{\Gamma_2}\frac{1}{\eta}\exp\left\{\frac{n\pi x}{(1+\eta^2)^{\frac{1}{2}}} + \frac{t}{\eta}\right\}d\eta,$$

which is to be evaluated around $\eta = 0$. The result is

$$2\pi i\sum_{m=0}^{\infty}\left(\frac{1}{m!}\right)^2\left[\frac{d^m}{d\eta^m}\exp\left\{\frac{n\pi x}{(1+\eta^2)^{\frac{1}{2}}}\right\}\right]_{\eta=0} t^m.$$

† For a sink located at points on the z axis other than the origin, the solution is similar, except for the dependence of a_n on n. The essential points of the subsequent discussion are unaffected by a specific choice of sink location.

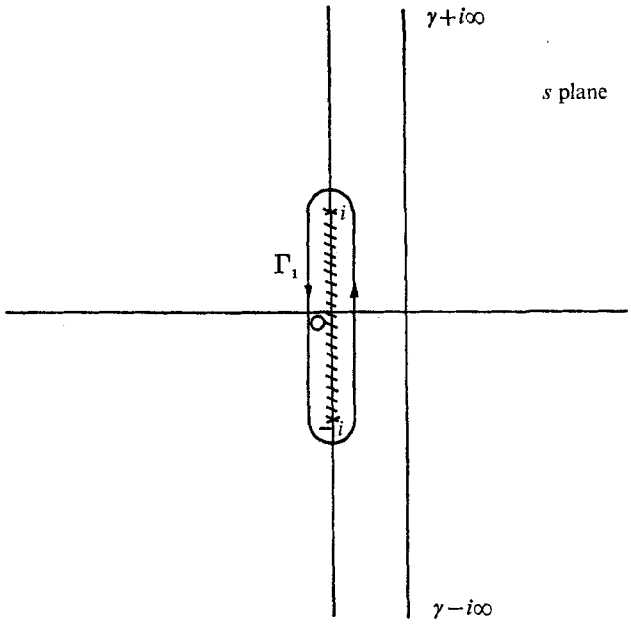

FIGURE 2. Contour around branch cut in s plane.

Substituting the above back into (10), we have

$$\psi^0(x,z,t) = z + \sum_{m=0}^{\infty}\sum_{n=1}^{\infty} \frac{2}{n\pi}\sin n\pi z \left(\frac{1}{m!}\right)^2 \left[\frac{d^m}{d\eta^m}\exp\left\{\frac{n\pi x}{(1+\eta^2)^{\frac{1}{2}}}\right\}\right]_{\eta=0} t^m$$

$$= z + \sum_{n=1}^{\infty}\frac{2}{n\pi}\sin n\pi z \exp(n\pi x)\left\{1 - \left(\frac{1}{2!}\right)^2 n\pi x t^2 + \left(\frac{1}{4!}\right)^2 [9n\pi x + 3(n\pi x)^2]t^4 - \left(\frac{1}{6!}\right)^2 [225n\pi x + 135(n\pi x)^2 + 15(n\pi x)^3]t^6 + \ldots\right\}. \quad (11)\dagger$$

The above series converges for all values of t; but the rate of convergence is extremely slow for large values of t. For small to moderate values of t, the series converges rapidly. The development of flow is illustrated by computing the solution in (11); it is shown in figure 3 for $t = 0{\cdot}5$, $2{\cdot}0$ and $3{\cdot}0$, which indicates the development of flow concentration through the compression of the streamlines. At $t = 3$ the upstream disturbance has propagated to just beyond $x = -1$, and a very weak eddy begins to make its appearance. The horizontal velocity profile at several x positions and different times is shown in figure 4, and a typical jet-like velocity profile is obtained at $x = -0{\cdot}4$, $t = 3$.

It is of interest to examine the nature of the propagation of disturbances. For sufficiently large times in the far field, $|\partial^2\psi/\partial z^2| \gg |\partial^2\psi/\partial x^2|$; thus (7) reduces to

$$\frac{\partial^2}{\partial t^2}\frac{\partial^2\psi}{\partial z^2} + \frac{\partial^2\psi}{\partial x^2} = 0, \quad (12)$$

† The developments leading to this solution were presented by Kao, Pao & Wei (1972).

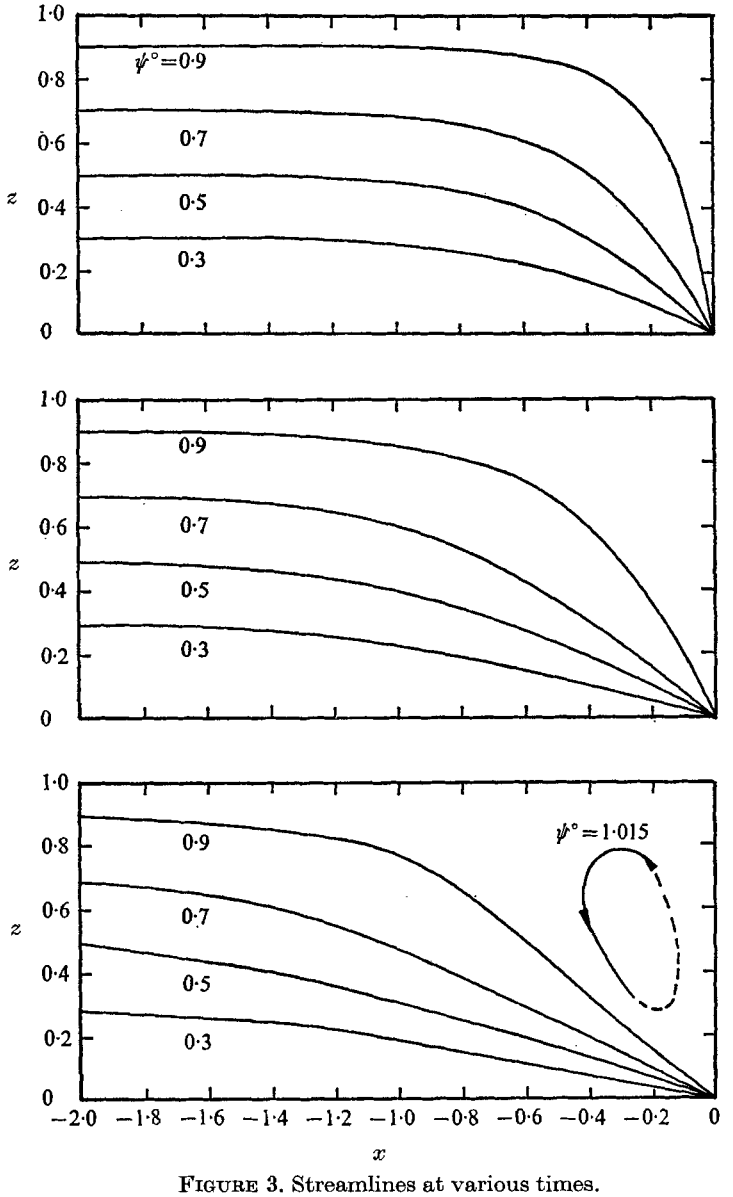

FIGURE 3. Streamlines at various times.

with the boundary and initial conditions for (7) remaining the same. Equation (12) can be solved by the same method used in solving (7), and the solution is

$$\psi(x,z,s) = \sum_{n=1}^{\infty} \frac{2}{n\pi} \sin n\pi z \left[\frac{1}{2\pi i} \int_{\gamma-i\infty}^{\gamma+i\infty} \frac{1}{s} \exp\{s(n\pi x + t)\}\, ds \right].$$

The only singularity of the above integral is located at $s = 0$ on the complex s plane, and the inversion is straightforward; thus we have

$$\psi(x,z,t) = \sum_{n=1}^{\infty} \frac{2}{n\pi} \sin n\pi z H(n\pi x + t), \tag{13}$$

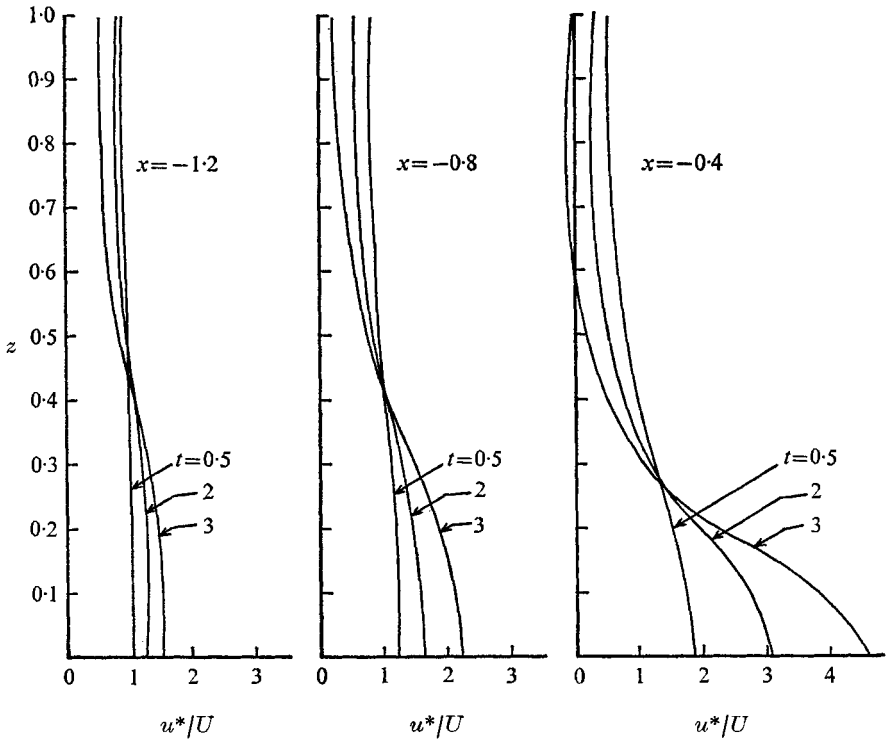

FIGURE 4. Horizontal velocity profile at various x and t.

$$\psi^0(x,z,t) = z + \sum_{n=1}^{\infty} \frac{2}{n\pi} \sin n\pi z H(n\pi x + t). \tag{14}$$

This result indicates clearly that the various modes of disturbance travel like waves at the velocity $c_n = 1/n\pi$, or in dimensional form

$$C_n = Nd/n\pi. \tag{15}$$

Such wave-like disturbance modes are called 'columnar disturbances' or 'columnar waves of zero frequency', since they propagate upstream in the form of horizontal jet-like columns.

The assumption $|\partial^2\Psi/\partial z^2| \gg |\partial^2\Psi/\partial x^2|$ or $|\partial u/\partial z| \gg |\partial w/\partial x|$ implies the hydrostatic condition in the vertical direction through the vorticity equation. This condition, in turn, is generally valid for long waves. Indeed ζ is now approximately equal to $\partial^2\Psi/\partial z^2$. Thus, from (3) and (4), the governing equations become

$$\frac{\partial^3\Psi}{\partial t\,\partial z^2} - \frac{\partial\rho}{\partial x} + F\left(\frac{\partial\Psi}{\partial z}\frac{\partial^3\Psi}{\partial x\,\partial z^2} - \frac{\partial\Psi}{\partial x}\frac{\partial^3\Psi}{\partial z^3}\right) = 0, \tag{16}$$

$$\frac{\partial\rho}{\partial t} + \frac{\partial\Psi}{\partial x} + F\left(\frac{\partial\rho}{\partial x}\frac{\partial\Psi}{\partial z} - \frac{\partial\rho}{\partial z}\frac{\partial\Psi}{\partial x}\right) = 0. \tag{17}$$

It may be readily seen that these nonlinear equations are satisfied by the solution

$$\Psi = \frac{1}{n\pi}\sin n\pi z\,\phi\left(x+\frac{t}{n\pi}\right),$$

$$\rho = -\sin n\pi z\,\phi\left(x+\frac{t}{n\pi}\right), \tag{18}$$

where ϕ is an arbitrary function. The above solution represents a mode of permanent form propagating with the velocity c_n in the negative x direction. In the linearized case, such modes may be superposed to satisfy the boundary condition at $x = 0$ yielding the solution in (14).

The simplified treatment just given helps us to focus our attention on the propagation of modes. The actual 'columnar disturbance' given by the linearized theory has a spatial structure given by the full solution (11). We may examine the spatial structure of each mode (i.e. for any fixed n) by computing the series in m as a function of $n\pi x$ for various values of t. Specifically, we compute the series

$$\sum_{m=0}^{\infty}\left(\frac{1}{m!}\right)^2\left[\frac{d^m}{d\eta^m}\exp\left\{\frac{n\pi x}{(1+\eta^2)^{\frac{1}{2}}}\right\}\right]_{\eta=0} t^m.$$

The centre-line horizontal component of velocity† due to the disturbance is then given by twice the value of the sum above. The result of this computation is shown in figure 5, where we have plotted this disturbance to the centre-line velocity u_m^*/U against $(n\pi x+t)$ for $t = 6$, 8 and 10. The figure shows, for any fixed time, the spatial structure of a disturbance mode. It is seen that the curves coincide for $(n\pi x+t) < 0$ (i.e. the forward tongue of the disturbance is indeed of permanent form). The zero on the abscissa corresponds to the point $|x| = t/n\pi = c_n t$ and may be regarded as the wave front. Behind the wave front, the wave does not have a permanent form and the wave disperses, and achieves the shape reminiscent of the Fresnel integral which is typical of dispersive waves.

In the regime where the linearized theory is valid, we may expect the disturbance modes to arrive one at a time and the solution is merely a superposition of the modes. However, since the whole flow field is moving towards the sink after initiation of the flow, only those disturbances with propagation speeds greater than the uniform speed Q/d can reach far upstream. Thus for $F = 0{\cdot}014$, say, only 22 modes can propagate upstream. From (18), it is expected that the same is true even in the nonlinear regime. Thus the higher the sink discharges the fewer the number of modes that can propagate upstream. If the discharge is such that $F \geqslant \pi^{-1}$, then the uniform flow speed is higher than that of the fastest-propagating mode (namely $n = 1$), there will be no upstream influence, and the solution of the kind found by Yih (1958) is applicable.

2.2. *The effect of viscosity and diffusivity*

It may be noted from the solution for the velocity field obtained in § 2.1 that, at a fixed x and for large t, the velocity gradient in z provided by the linearized theory becomes increasingly large, owing to the unattenuated arrival of more and

† That is, the velocity along the x axis at the level of the sink.

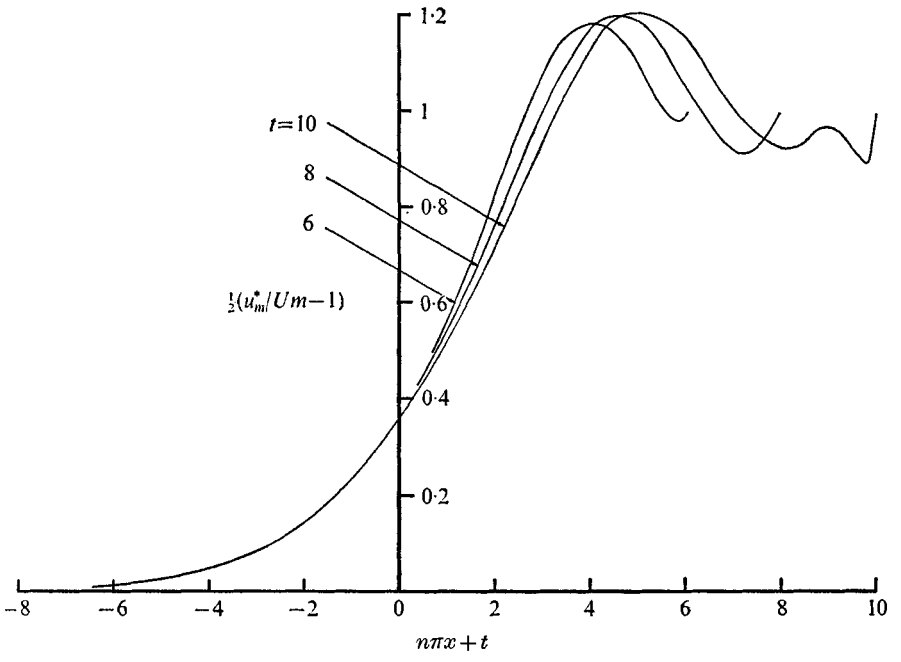

FIGURE 5. Spatial structure of a disturbance mode.

more modes. Indeed, from (14), the asymptotic limit of ψ^0 as $t \to \infty$, for any x, is $\psi^0 = 1$ or $\partial\psi^0/\partial z = \delta(z)$, where $\delta(z)$ is the Dirac delta function. This may also be seen by applying the Tauberian theorem for $t \to \infty$ to (8). Thus viscous influences are no longer negligible. We may include viscous influence (without diffusion), to some extent, by making a boundary-layer type assumption (i.e. $\partial^2/\partial z^2 \gg \partial^2/\partial x^2$); the linearized vorticity equation then assumes the form

$$\frac{\partial}{\partial t^2}\frac{\partial^2\psi}{\partial z^2} + \frac{\partial^2\psi}{\partial x^2} = \epsilon \frac{\partial}{\partial t}\frac{\partial^4\psi}{\partial z^4},$$

where $\epsilon = \nu/Nd^2$ is the dimensionless viscosity coefficient. We may examine the attenuation of each mode $A_n(x,t)\sin(n\pi z)$ separately. The equation governing A_n is

$$\frac{\partial^2 A_n}{\partial t^2} - \frac{1}{n^2\pi^2}\frac{\partial^2 A_n}{\partial x^2} + \epsilon n^2\pi^2 \frac{\partial A_n}{\partial t} = 0.$$

For $\epsilon \gg (n^4\pi^4)^{-1}$, we have $A_n = a_n \exp\{-\epsilon n^2\pi^2 t\}$, or the amplitude attenuates exponentially with t. Since the disturbance travels with a speed $1/n\pi$, the spatial attenuation of the amplitude as a disturbance propagates upstream is given by $\exp(\epsilon n^3\pi^3 x), x < 0$. If we now assume that this is the viscous damping factor for all modes, then the steady-state solution is

$$\psi^0 \simeq z + \sum_{n=1}^{\infty} \frac{2}{n\pi}\sin(n\pi z)\exp(\epsilon n^3\pi^3 x), \quad x < 0, \tag{19}$$

which closely resembles the solution of Imberger (1972), and that of Koh (1966*a*) for an infinite medium.

If we also retain the effect of diffusion, the linearized vorticity equation becomes

$$\frac{\partial^2}{\partial t^2}\frac{\partial^2 \psi}{\partial z^2} - (\epsilon + D')\frac{\partial^5 \psi}{\partial t\,\partial z^4} + \frac{\partial^2 \psi}{\partial x^2} + \epsilon D'\frac{\partial^6 \psi}{\partial z^6} = 0,$$

where D' is the diffusivity D normalized by Nd^2. The solution by Laplace transforms satisfying the slip boundary conditions (i)–(iii) of equation (7) is

$$\overline{\psi} = \sum_{n=1}^{\infty} \frac{2}{n\pi} \sin n\pi z \exp\{(s^2 + s(\epsilon + D')\, n^2\pi^2 + \epsilon D' n^4\pi^4)^{\frac{1}{2}}\, n\pi x\}.$$

On using the Tauberian theorem for $t \to \infty$, we get the steady-state solution for the zeroth-order linearized problem

$$\psi(x, z, t = \infty) = \sum_{n=1}^{\infty} \frac{2}{n\pi} \sin(n\pi z) \exp\{(\epsilon D')^{\frac{1}{2}} n^3\pi^3 x\}, \quad x < 0,$$

or

$$\psi^0(x, z, t = \infty) = z + \sum_{n=1}^{\infty} \frac{2}{n\pi} \sin(n\pi z) \exp\{\epsilon D')^{\frac{1}{2}} n^3\pi^3 x\}, \quad x < 0, \tag{20}$$

which agrees with Imberger's (1972) solution exactly.

2.3. *Calculation of the density field*

The solution for the density field can be obtained similarly. Upon calculation, it may be shown that

$$\rho^0(x < 0, z, t) = -\frac{2}{\pi} \sum_{n=1}^{\infty} \beta_n \sin \beta_n z \sum_{m=0}^{\infty} 2\pi i \frac{(-1)^m t^{2m+1}}{(2m+1)!\, m!} \times \frac{d^m}{d\alpha^m}\left[\frac{\alpha^{2m} \exp\{-i\alpha x\}}{(\alpha^2 + \beta_n^2)^{m+1}}\right]_{\alpha = i\beta_n}, \quad \beta_n \equiv n\pi. \tag{21}$$

Figure 6 shows the lines of constant perturbation density as time increases, and the penetration of the disturbance upstream. The penetration progresses on a time scale of the order of $1/N$, which was predicted, and is shown by (15).

3. Numerical solution

3.1. *Formulation*

For higher values of F and longer times, it is seen that nonlinear effects become important. The full Navier–Stokes equations, incorporating both viscosity and diffusivity, will now be solved numerically by a finite-difference scheme. The governing equations for a viscous, diffusive, stably stratified Boussinesq fluid in dimensionless form are

$$\frac{\partial \gamma}{\partial \tau} + \frac{\partial}{\partial x}(u\gamma) + \frac{\partial}{\partial z}(w\gamma) = Sc^{-1} Re^{-1}\left(\frac{\partial^2 \gamma}{\partial x^2} + \frac{\partial^2 \gamma}{\partial z^2}\right), \tag{22}$$

$$\frac{\partial \zeta}{\partial \tau} + \frac{\partial}{\partial x}(u\zeta) + \frac{\partial}{\partial z}(w\zeta) = F^{-2}\frac{\partial \gamma}{\partial x} + Re^{-1}\left(\frac{\partial^2 \zeta}{\partial x^2} + \frac{\partial^2 \zeta}{\partial z^2}\right), \tag{23}$$

$$\frac{\partial^2 \Psi}{\partial z^2} + \frac{\partial^2 \Psi}{\partial z^2} = \zeta, \tag{24}$$

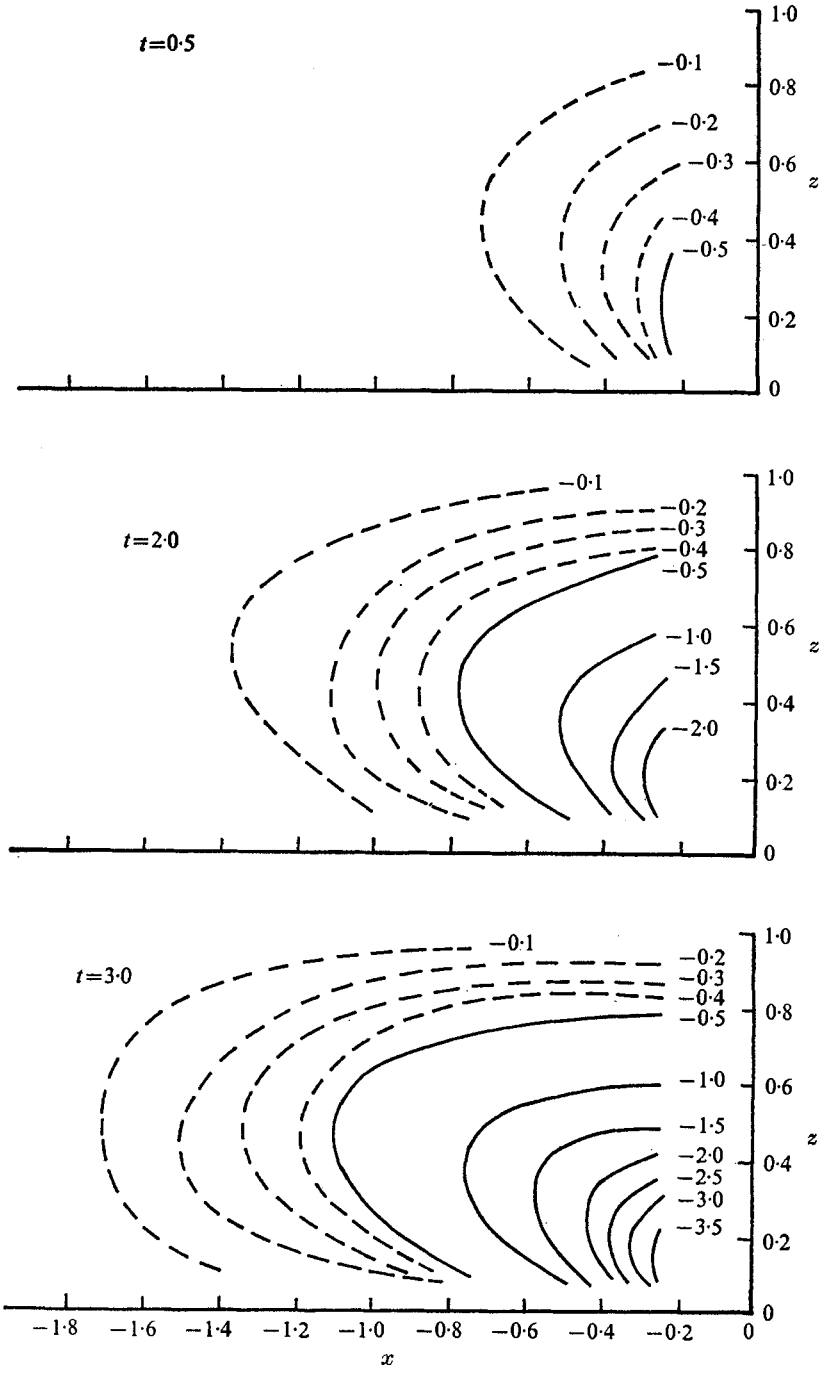

FIGURE 6. Isopycnic lines for the perturbation density at various t.

where

$$\left.\begin{aligned} \zeta = \frac{\partial u}{\partial z} - \frac{\partial w}{\partial x}, \quad u = \frac{\partial \Psi}{\partial z}, \quad w = -\frac{\partial \Psi}{\partial x}, \\ \tau = \frac{TQ}{d^2}, \quad \gamma = \frac{\rho^* - \rho_0}{\rho_0 - \rho_s}, \\ F = \frac{Q}{Nd^2}, \quad Re = \frac{Q}{\nu}, \quad Sc = \frac{\nu}{D}. \end{aligned}\right\} \tag{25}$$

Equations (22) and (23) are essentially the same as (2) and (1), except that the viscous and diffusive terms are now included. It is seen that the time scale based on the discharge Q is used here. However, the conversion between τ and t can easily be done with $\tau/t = F$. The dimensionless density γ is so defined here that any initial density stratification can be used although only linear stratification is considered in this paper.

Initial and boundary conditions. Since the initial and boundary conditions are such that γ, w, ζ and Ψ are all odd functions of z, while u is an even function of z, it is readily seen from (22)–(24) that they will remain odd functions of z, and that u will remain an even function of z, as time goes on. The flow and density fields will be symmetric about the line $x = 0$ at all times. Therefore, in the numerical computation it is convenient to consider only the first quadrant of x, z space, where both x and z are positive.

The initial solution for a sudden start of a sink discharge at the origin is a potential flow given by

$$\left.\begin{aligned} \Psi &= -z - \frac{2}{\pi} \sum_{n=1}^{\infty} \frac{1}{n} \exp(-n\pi x) \sin n\pi z \\ \zeta &= 0 \\ \gamma &= -z \end{aligned}\right\} \quad \text{for} \quad t = 0, \quad x > 0. \tag{26}$$

Since Ψ, ζ and γ will remain odd functions of z, it follows that

$$\Psi = 0, \quad \zeta = 0, \quad \gamma = 0 \quad \text{at} \quad z = 0.$$

At $z = 1$ we have $\Psi = -1$. To avoid a thin viscous boundary layer at $z = 1$, a slip condition is imposed here. In that case, we consider that there exists a series of line sinks located along the line $x = 0$ at intervals two non-dimensional lengths from each other (as shown in figure 7). Using a similar argument for $z = 0$, it can be shown that $\Psi + 1$, $\gamma + 1$ and ζ will remain odd functions about $z = 1$. Hence, the boundary conditions at $z = 1$ are $\Psi = -1$, $\gamma = -1$, $\zeta = 0$. The boundary conditions at $x = 0$ are $\Psi = -1$, $\zeta = 0$ and $\partial\gamma/\partial x = 0$, owing to symmetry there. At $x = \infty$, the flow and density field remain undisturbed during any finite time, since disturbances travel at finite speeds. The boundary conditions are now summarized in figure 8.

3.2. *Numerical procedure*

The solution of (22)–(25) is accomplished by writing these equations in a finite-difference form, and solving them on a digital computer, according to the following algorithm.

(i) At $t = 0$ the initial conditions (26) prevail. (ii) The u and w velocity fields

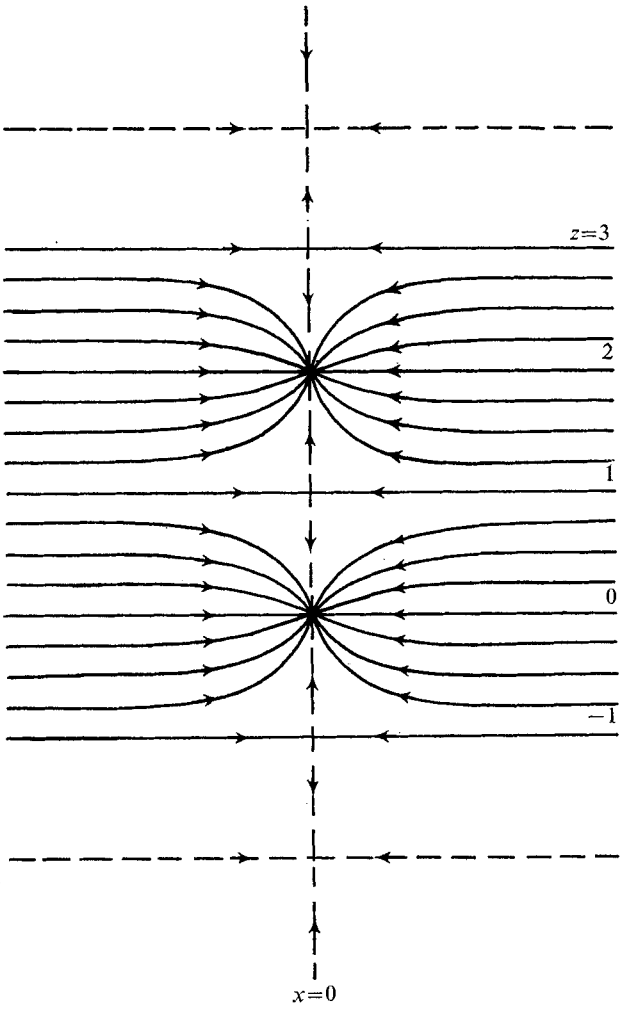

FIGURE 7. Schematic drawing of a series of sinks located along the line $x = 0$.

at $t = 0$ are computed from (25). (iii) Equation (22), subject to the appropriate boundary conditions (see figure 8), is used to make a time step in the density field γ. (iv) Equation (23) is used to make a time step in the vorticity field ζ. (v) With the new result for the vorticity field, a new value for the Ψ field is computed by over-relaxing (24), subject to the appropriate boundary conditions. (vi) The u and w velocity fields are then updated from this new field by using (25). Steps (iii)–(vi) are repeated until a specified time $t = t_f$ is reached. The computer can be requested to print out the Ψ, γ, ζ, u and w fields at $t = 0$, $t = t_f$, and at any specified intermediate times, so that the time development of the flow field and wave motion can be studied.

The flow field has a singularity at the origin where the flow speed becomes infinite, causing numerical instability. To circumvent this difficulty, a small horizontal opening of finite length is used, through which a uniform flow is

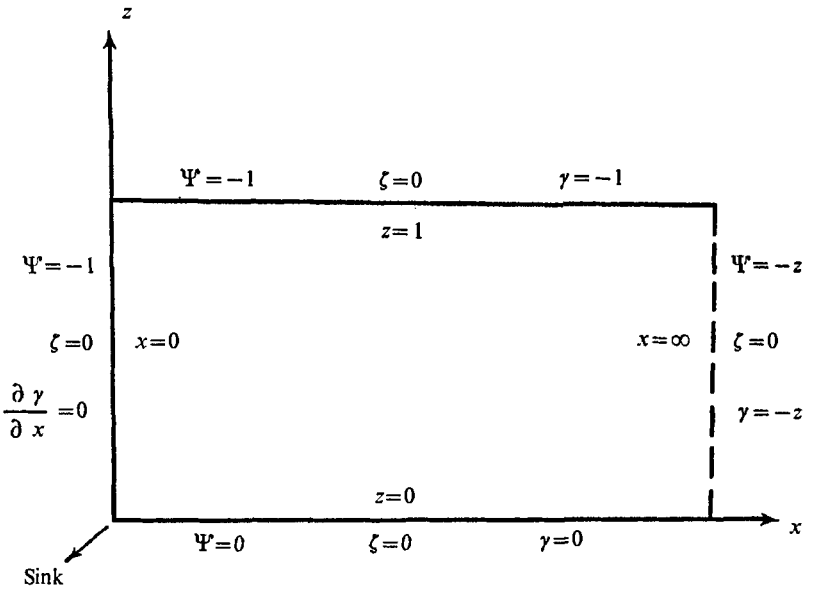

FIGURE 8. Boundary conditions.

discharged. It turns out that the flow and density fields are not sensitive to the length of the opening, as long as the opening length remains small. The sink opening was taken to be twice the horizontal grid length, in all the numerical computations. The initial field is then slightly different from the solution in (26). This can be obtained by first making an initial guess for Ψ, using the solution in (26), then converging to the correct result by over-relaxation of (24), with no vorticity term. The convergence is quite rapid.

3.3. *Stretched co-ordinate system*

The present problem involves a boundary at infinity. A dilemma is posed by the conflicting requirements of keeping the finite-difference grid mesh fine in the vicinity of the sink, where the gradients are largest, and at the same time having the last grid point far enough away from the sink that it is a close approximation to infinity. In the initial phase of the computation, we used unstretched co-ordinates, with the upstream boundary set at a reasonably large distance from the sink. We found that, whenever the fastest-propagating disturbance (columnar wave of the first mode) reached this upstream boundary, a partial reflexion was inevitable, although a scheme was devised to absorb the wave. Thus, the flow field at a given section invariably entailed some error, as soon as the reflected wave passed this section.

We seek a co-ordinate system $(\bar{x}, \bar{z})$ whose mapping to ordinary Cartesian co-ordinates (x, z) is such that $\bar{x}$ varies from 0 to $+1$ as x varies from 0 to $+\infty$. The transformation for such a system is given by

$$\bar{x} = 1 - \exp(-ax), \quad \bar{z} = z, \tag{27}$$

where a is a scale factor. On substituting the transformation relation (27) into the governing equations (22)–(24), we obtain

$$\frac{\partial\gamma}{\partial\tau}+a(1-\bar{x})\frac{\partial}{\partial\bar{x}}(u\gamma)+a(1-\bar{x})\frac{\partial}{\partial z}(w_1\gamma)$$

$$=Sc^{-1}Re^{-1}\left[a^2(1-\bar{x})^2\frac{\partial^2\gamma}{\partial\bar{x}^2}-a^2(1-\bar{x})\frac{\partial\gamma}{\partial\bar{x}}+\frac{\partial^2\gamma}{\partial z^2}\right], \tag{28}$$

$$\frac{\partial\zeta}{\partial\tau}+a(1-\bar{x})\frac{\partial}{\partial\bar{x}}(u\zeta)+a(1-\bar{x})\frac{\partial}{\partial z}(w_1\zeta)$$

$$=F^{-2}a(1-\bar{x})\frac{\partial\gamma}{\partial\bar{x}}+Re^{-1}\left[a^2(1-\bar{x})^2\frac{\partial^2\zeta}{\partial\bar{x}^2}-a^2(1-\bar{x})\frac{\partial\zeta}{\partial\bar{x}}+\frac{\partial^2\zeta}{\partial z^2}\right], \tag{29}$$

$$a^2(1-\bar{x})^2\frac{\partial\Psi}{\partial\bar{x}^2}-a^2(1-\bar{x})\frac{\partial\Psi}{\partial\bar{x}}+\frac{\partial^2\Psi}{\partial z^2}=\zeta, \tag{30}$$

where $$w_1=-\partial\Psi/\partial\bar{x}.$$

The main reason for choosing (27) as the transformation relation is that Δx remains small near the origin, while it increases as x increases. By choosing the scale factor properly, Δx can be made equal to 0·1 near the origin, while Δx invariably becomes very large as x approaches infinity. Since in the present initial-value problem the disturbances are initiated at the origin and gradually propagated upstream toward large x, they would take some considerable time to penetrate far upstream, unless F is extremely small. Therefore, the finite-difference equations remain accurate until the disturbances reach the final few grid points near $x=\infty$ where the grid spacings are large. At that time, steady state is established for small and moderate values of x.

3.4. *Finite-difference equations*

For finite differencing, a central difference in space and forward difference in time are used, except in the case of the nonlinear terms, for which the special three-point non-central differencing method (Torrance & Rockett 1969) is adopted. Equations (28) and (29) are parabolic, while (30) is elliptic and solved by the standard over-relaxation technique. The subscripts i and j denote the space point in the $\bar{x}$ and z directions, respectively; and a prime denotes the new time point. For given values of i and j, the space co-ordinates are $\bar{x}=i\Delta\bar{x}$, $z=j\Delta z$. With the foregoing notation, (28)–(30) may be written in the finite-difference form

$$\frac{\gamma'_{i,j}-\gamma_{i,j}}{\Delta\tau}=-a(1-\bar{x})\left[\frac{\bar{u}_{i,j}\gamma_{i,j}-\bar{u}_{i-1,j}\gamma_{i-1,j}}{\Delta\bar{x}}+\frac{\bar{w}_{i,j}\gamma_{i,j}-\bar{w}_{i,j-1}\gamma_{i,\,j-1}}{\Delta z}\right]$$

$$+Sc^{-1}Re^{-1}\left[a^2(1-\bar{x})^2\frac{\gamma_{i+1,j}+\gamma_{i-1,j}-2\gamma_{i,j}}{(\Delta\bar{x})^2}-a^2(1-\bar{x})\frac{\gamma_{i+1,j}-\gamma_{i-1,j}}{2\Delta\bar{x}}\right.$$

$$\left.+\frac{\gamma_{i,j+1}+\gamma_{i,j-1}-2\gamma_{i,j}}{(\Delta z)^2}\right], \tag{31}$$

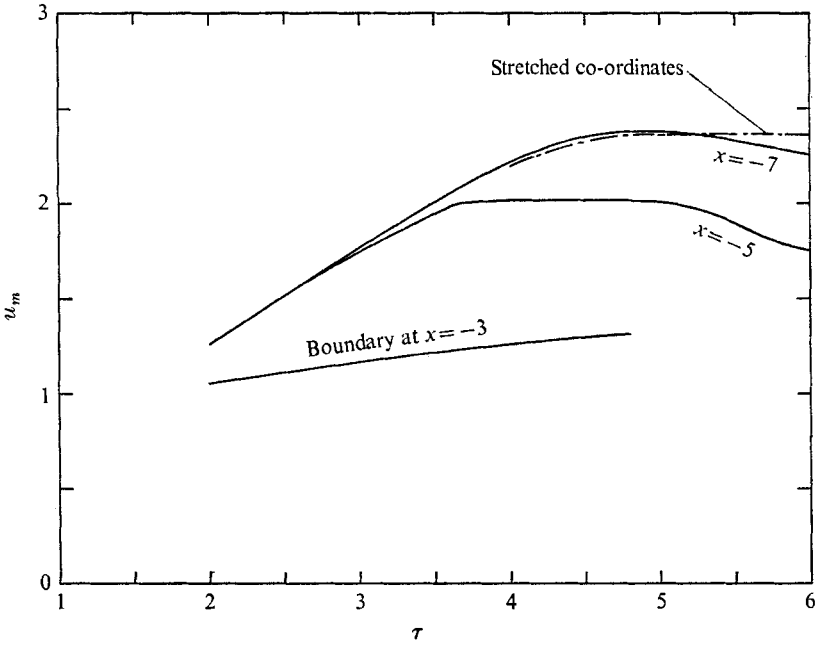

FIGURE 9. The centre-line velocity at $x = -3{\cdot}0$ for $F = 0{\cdot}15$. A comparison between the numerical results obtained from stretched and unstretched co-ordinates.

$$\frac{\zeta'_{i,j}-\zeta_{i,j}}{\Delta\tau} = -a(1-\bar{x})\left[\frac{\bar{u}_{i,j}\zeta_{i,j}-\bar{u}_{i-1,j}\zeta_{i-1,j}}{\Delta\bar{x}}+\frac{\bar{w}_{i,j}\zeta_{i,j}-\bar{w}_{i,j-1}\zeta_{i,j-1}}{\Delta z}\right]$$
$$+F^{-2}a(1-\bar{x})\frac{\gamma_{i+1,j}-\gamma_{i-1,j}}{2\Delta\bar{x}}+Re^{-1}\left[a^2(1-\bar{x})^2\frac{\zeta_{i+1,j}+\zeta_{i-1,j}-2\zeta_{i,j}}{(\Delta\bar{x})^2}\right.$$
$$\left.-a^2(1-\bar{x})\frac{\zeta_{i+1,j}-\zeta_{i-1,j}}{2\Delta\bar{x}}+\frac{\zeta_{i,j+1}+\zeta_{i,j-1}-2\zeta_{i,j}}{(\Delta z)^2}\right], \tag{32}$$

$$\psi_{i,j}^{(s+1)} = (1-A)\psi_{i,j}^{(s)}+A\{4a^2(1-\bar{x})^2(\Delta z)^2+4(\Delta\bar{x})^2[-2(\Delta\bar{x})^2(\Delta z)^2\zeta_{i,j}$$
$$+a^2(1-\bar{x})(\Delta z)^2(2(1-\bar{x})(\psi_{i+1,j}+\psi_{i-1,j})-\Delta\bar{x}(\psi_{i+1,j}-\psi_{i-1,j}))$$
$$+2(\Delta\bar{x})^2(\psi_{i,j+1}+\psi_{i,j-1})]\}, \tag{33}$$

where
$$u_{i,j} = (\psi_{i,j+1}-\psi_{i,j-1})/2(\Delta z),$$
$$w_{1i,j} = (\psi_{i-1,j}-\psi_{i+1,j})/2(\Delta\bar{x}),$$
$$\bar{u}_{i,j} = \tfrac{1}{2}(u_{i+1,j}+u_{i,j}), \quad \bar{w}_{i,j} = \tfrac{1}{2}(w_{1i,j}+w_{1i+1,j}).$$

The expressions for the nonlinear terms are for the case $\bar{u}_{i,j} \geqslant 0$, $\bar{u}_{i-1,j} \geqslant 0$, $\bar{w}_{i,j} \geqslant 0$ and $\bar{w}_{i,j-1} \geqslant 0$. Expressions for other cases can similarly be made following Torrance & Rockett (1969).

3.5. *Numerical results*

To compare the numerical computations with the theoretical results in the preceding sections and the experimental results in part 2, all the numerical results are presented in the second quadrant of x, z space, where x is negative.

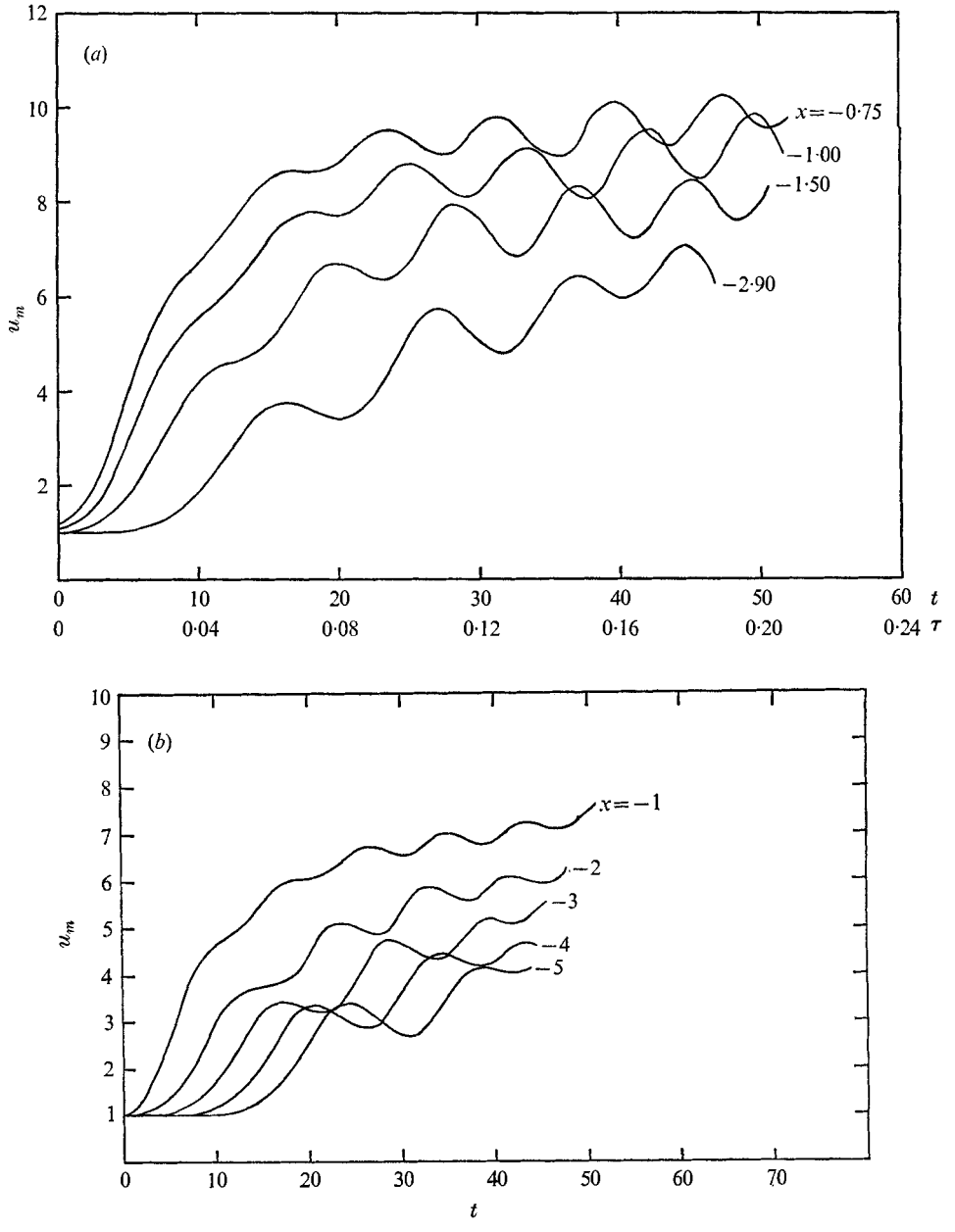

FIGURES 10(*a*), (*b*). For legend see next page.

Various Reynolds numbers were used, ranging from 20 to 10^6. For most computations, Schmidt numbers (ν/D) with values of 10 and 1000 were used, which approximately correspond to the temperature diffusion and salinity diffusion in water, respectively. Over ten values of the Froude number were used, ranging from 0·32 to 0·004. For all cases, Δz was chosen to be 0·05, which corresponds to 20 equal grid spacings in the z direction. In the x direction, various grid sizes

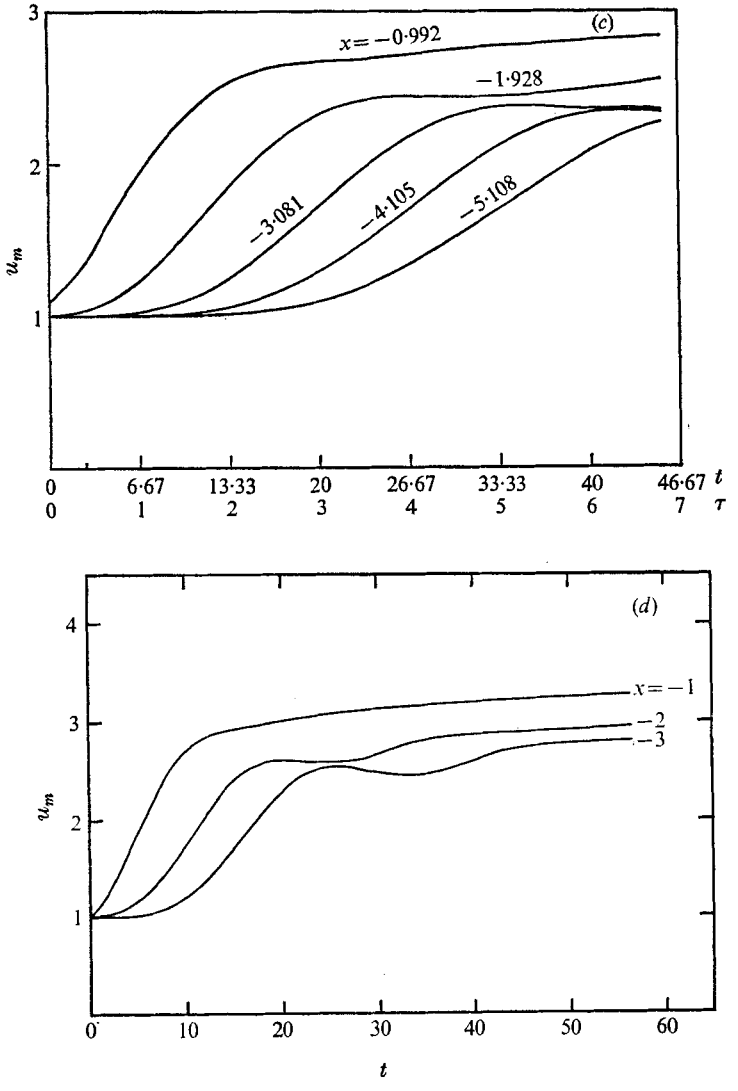

FIGURE 10. Numerical solution for the growth of centre-line velocity with time at various x. ——, numerical solution.

	F	Re	Sc
(*a*)	0·004	20	7·14
(*b*)	0·0145	625	1000
(*c*)	0·15	10^6	833
(*d*)	0·106	3400	833

were used, depending on the Froude number. For $F = 0{\cdot}014$, 80 grid spacings in the $\bar{x}$ direction are needed, while, for $F \geqslant 0{\cdot}20$, 40 grid spacings are sufficient.

To see the necessity of introducing the stretched co-ordinates, we give a typical example. For $F = 0{\cdot}15$, the centre-line velocity $u_m = u_m^*/U$ at the vertical section $x = -3$ is plotted against the time τ (as shown in figure 9). In the initial phase of the numerical computation, unstretched co-ordinates were used, with

τ	x	c_A	c
0·075	−1·8		
		21·3	22·3
0·150	−3·4		
		21·3	22·3
0·225	−5·0		
		21·2	22·2
0·275	−6·06		

TABLE 1. Numerical values of the wave velocity of the first disturbance mode for $F = 0{\cdot}014$

the upstream boundary set at $x = -3$, $x = -5$ or $x = -7$ ($\Delta x = 0{\cdot}1$ for all the cases). Figure 9 shows that u_m deviates from its true value as soon as the reflected wave reaches the section $x = -3$. On the other hand, the stretched co-ordinates with 40 grid spacings in the x direction do not have the ill effect of the reflected waves; u_m increases with τ until $\tau = 4{\cdot}8$, when it approaches a steady state.

On careful examination of the flow development from the numerical results, it is indeed confirmed that the successive arrival of columnar disturbance modes can be identified as the mechanism responsible for the development of flow concentration in the withdrawal region. Figures 10(*a*)–(*c*) show the growth of centre-line velocity with time at various x for $F = 0{\cdot}004$, 0·0143 and 0·15, respectively. For the low Froude numbers, one can see clearly the arrival and peaking of each mode. For $F = 0{\cdot}004$ ($Re = 20$, $Sc = 7{\cdot}14$) one can see the arrival and peaking of the first two modes, which are a linear superposition of the first two modes predicted by the linear theory (cf. figure 5 and its extrapolation to larger t). By the time the third and higher modes arrive, the nonlinear interaction and viscous damping of these columnar disturbance modes become important, although the qualitative features of the linear theory remain valid for this very small value of F. For $F = 0{\cdot}15$, steady state is almost reached for $|x| \leqslant 4$ at the time $\tau = 6{\cdot}0$. There is essentially no attenuation of the centre-line velocity between $x = -3$ and $x = -4$. The passage to steady state is further illustrated in figure 10(*d*) for $F = 0{\cdot}106$. It is seen that the centre-line velocity remains constant for all $t > 50$ ($\tau > 5{\cdot}3$) for all $x < 3$ (i.e. the flow is steady for $x < 3$ when $t > 50$). Comparison of the numerical with the experimental results for various F's will be given in part 2. To see how the waves penetrate upstream, the centre-line velocity for $F = 0{\cdot}014$ is plotted against x, with the time τ as a parameter (in figure 11). Again, for this low F, the spatial structure of the first disturbance mode is essentially the same as that predicted by the linear theory (as in figure 5). The forward tongue of the disturbance is indeed of permanent form. If we now focus our attention on the first mode, with $u_m = 1{\cdot}5$, the times and locations when such a disturbance mode arrives are tabulated in table 1. The advancing speed c_A can then be calculated between each interval. Since the wave is advancing upstream against a basic current with average velocity equal to unity, the true velocity relative to the medium would then be $c_A + 1{\cdot}0$, which is shown in

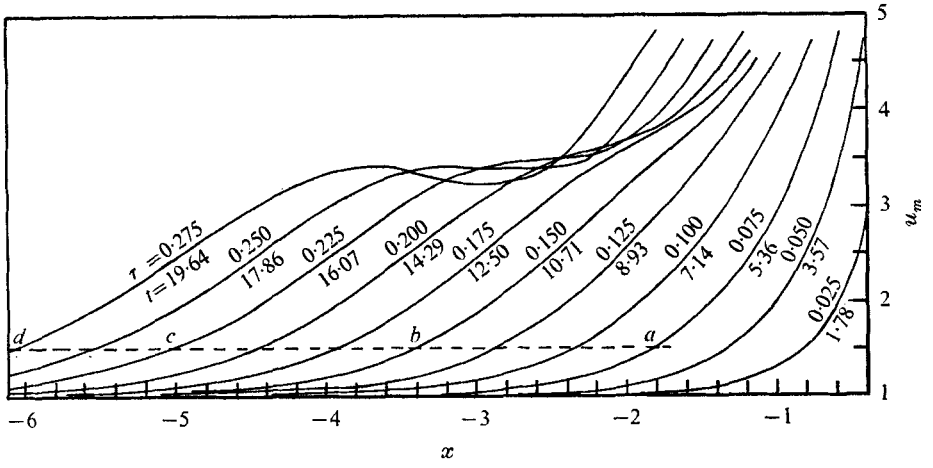

FIGURE 11. Centre-line velocity u_m against position x, showing the spatial structure of the disturbance at various τ, for $F = 0{\cdot}014$, $Re = 625$, $Sc = 833$.

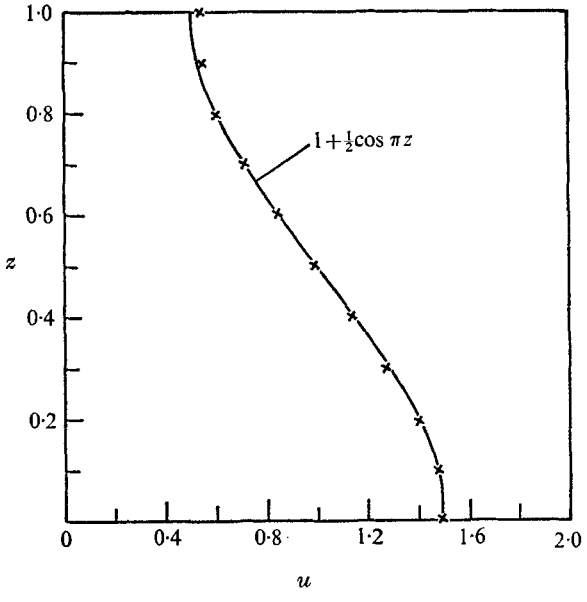

FIGURE 12. Comparison of the first mode analytic solution $u = 1 + \frac{1}{2}\cos\pi z$ with the numerical solution x at space-time points a–d, as shown in figures 11 and 13, for $F = 0{\cdot}014$ and $0{\cdot}20$.

the last column of table 1. This wave velocity is to be compared with the columnar wave speed of the first mode, which is 22·7. Therefore, at this low F, the first mode essentially propagates with the speed derived from the linear theory. Moreover, the horizontal velocity profiles at points b–d are almost indistinguishable, while there is only a very slight deviation at point a. The velocity profile is plotted in figure 12. It is seen that this velocity profile fits the curve

$$u = 1 + \tfrac{1}{2}\cos\pi z$$

τ	x	c_A	c
3·2	−2·2		
		0·538	1·538
4·8	−3·06		
		0·525	1·525
6·4	−3·9		
		0·406	1·406
9·6	−5·2		

TABLE 2. Numerical values of the wave velocity of the first disturbance mode for $F = 0{\cdot}20$

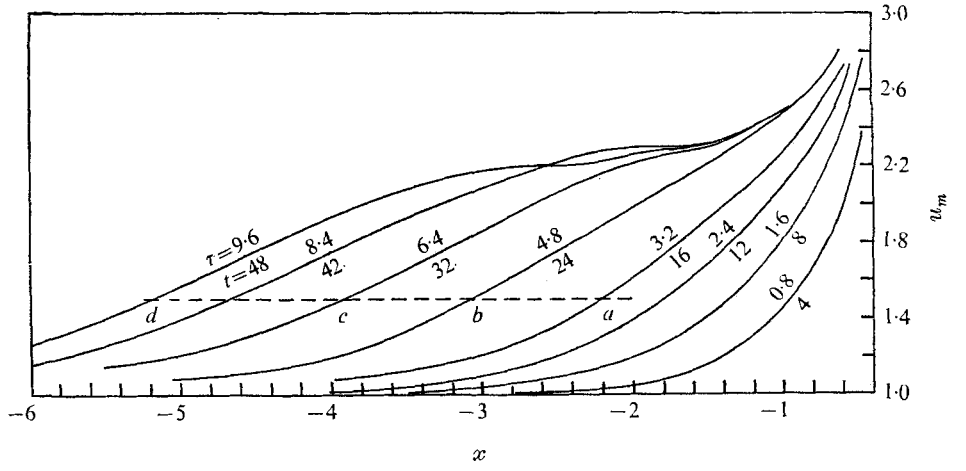

FIGURE 13. Centre-line velocity u_m against position x, showing the spatial structure of the disturbance at various time τ, for $F = 0{\cdot}20$, $Re = 10\,000$, $Sc = 1000$.

very well. This is, of course, not surprising, since it is exactly the shape of the first disturbance mode. Therefore, it is clear now that the forward tongue of the disturbance is indeed of permanent form, and propagates with a speed predicted by the linear theory. Now consider the case for which $F = 0{\cdot}20$. A plot like that of figure 11 is shown in figure 13. In this case it is seen that only one disturbance mode can penetrate upstream. Again let us focus our attention on the first mode with $u_m = 1{\cdot}5$. The times and locations for the arrival of the disturbance are tabulated in table 2. The wave velocity relative to the medium is listed in the last column, which is to be compared with the columnar wave speed of 1·59. The slight discrepancy is probably due to the fact that the basic current is no longer uniform as the wave progresses upstream. However, the horizontal velocity profiles at points *a*–*d* are almost indistinguishable from the expression $u = 1 + \frac{1}{2}\cos \pi z$. In other words, the forward tongue of the disturbance is again of permanent form, and advances at approximately the wave speed predicted by the linear theory. This is not surprising in view of (18), where the solutions are shown to satisfy the nonlinear equations, provided $|\partial^2\Psi/\partial z^2| \gg |\partial^2\Psi/\partial x^2|$, and provided only one mode is present. These provisions are precisely satisfied in the advancing tongue of the first mode for any $F < \pi^{-1}$. Therefore, the present

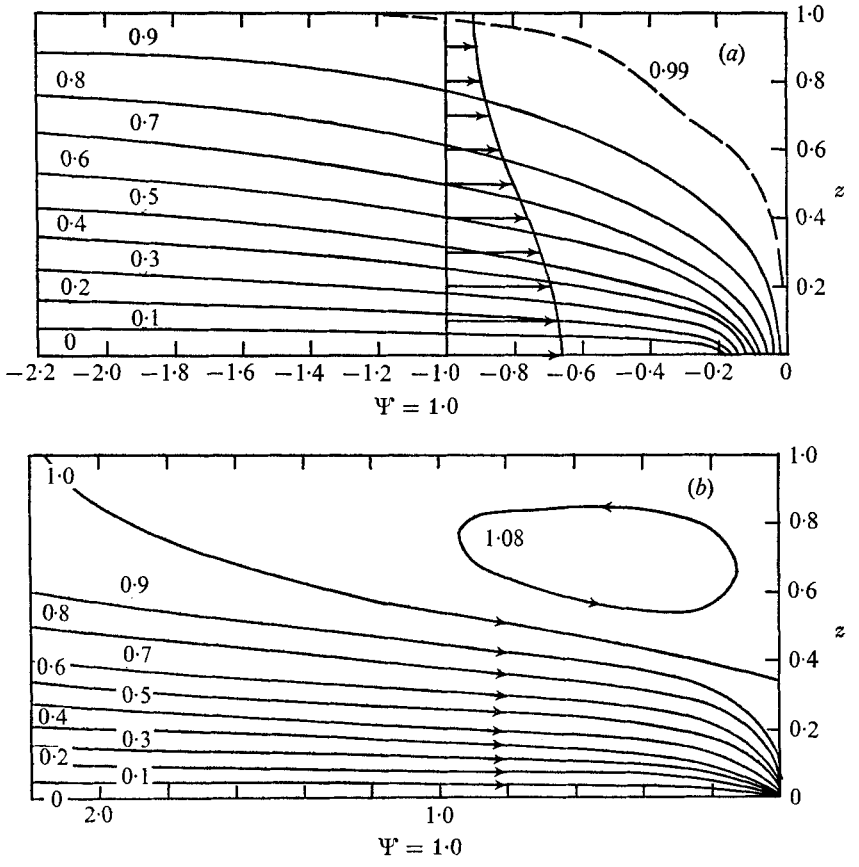

FIGURE 14. Steady-state pattern for $F = 0{\cdot}32$, $Re = 10\,000$, $Sc = 1000$. (*a*) Numerical solution. (*b*) Yih's solution.

linear theory can very well predict the progress of disturbance modes and the permanent form of the forward tongue, and, for sufficiently small values of F (less than 10^{-2}), the development of the flow field for a reasonable interval of time. But it cannot give the steady-state flow profile, except for $F \to 0$, since then nonlinear effects become important.

The effect of Reynolds number or viscosity on the numerical solutions is now discussed briefly. For small F (say $F = 0{\cdot}014$), the corresponding Reynolds number is $O(10^2)$ and viscous effects contribute to the attenuation of the higher modes. At higher F and higher Re, the influence of viscosity is no longer important for $|x| < 5$. The solution remains essentially the same, with several orders of magnitude increase in Re. The effect of changes in diffusivity on the flow and density fields is also very small. For example, numerical solutions for $F = 0{\cdot}15$ have been computed for $Re = 10^4$ and $Sc = 10$, and $Re = 10^6$ and $Sc = 833$. The flow and density fields are found to be almost indistinguishable between these two cases at all times (in general, the computation was terminated before the steady state was reached for $|x| > 4$). This shows that the flow and density fields are independent of Re and $Re\,Sc$, provided these two values are large. Similar results

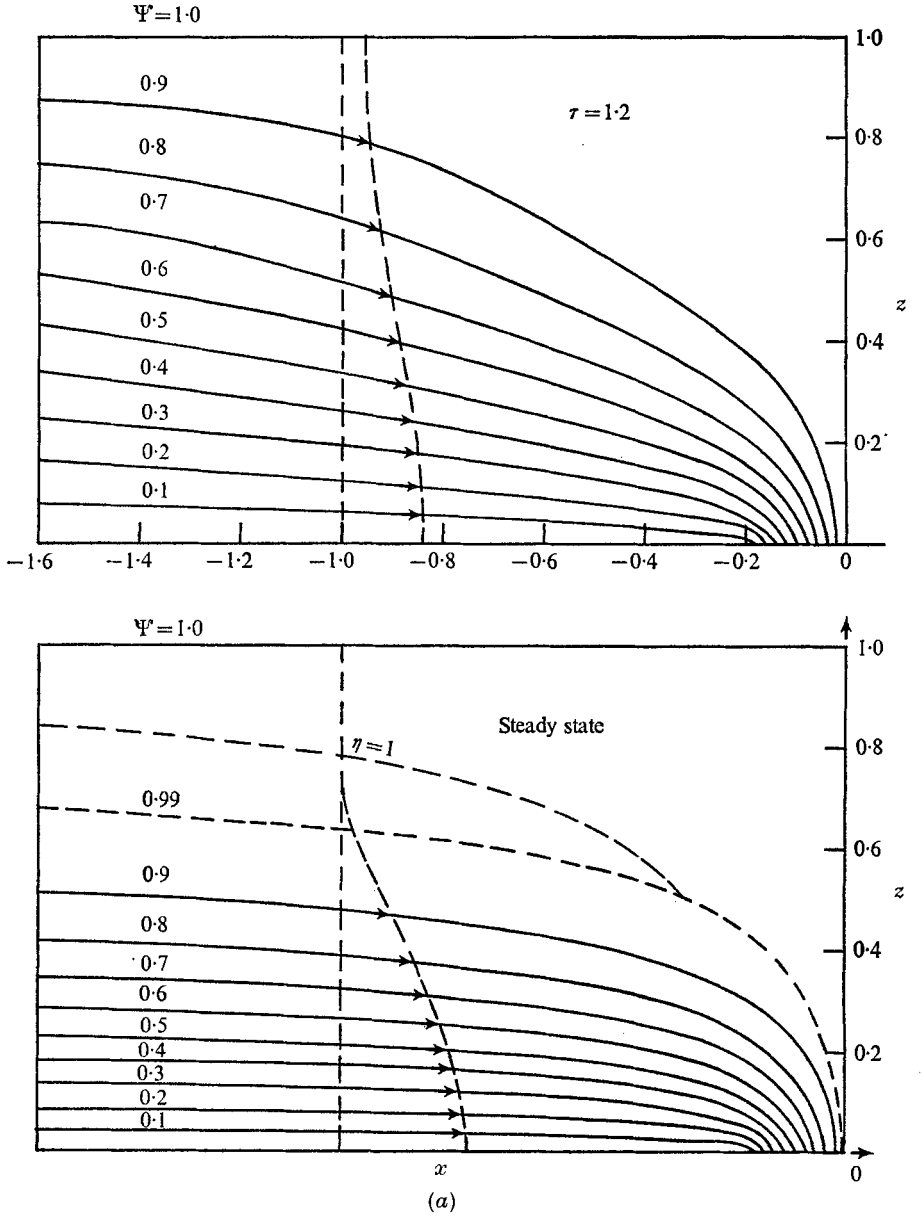

(a)

FIGURE 15(a). For legend see facing page.

were obtained for other values of F, ranging from 0·32 to 0·0713. Thus the establishment of the flow and density fields is essentially inviscid and non-diffusive for the range $F > 0{\cdot}07$ and $Re > 10^4$ (with $Sc > 1$).

As mentioned above, a numerical computation for $F = 0{\cdot}32$ was also made for which F was slightly above the critical value π^{-1}. It is seen that no wave can propagate upstream, and that the flow remains uniform far upstream, in agreement with Yih (1958, 1965). A steady-state flow pattern is shown in figure 14(a).

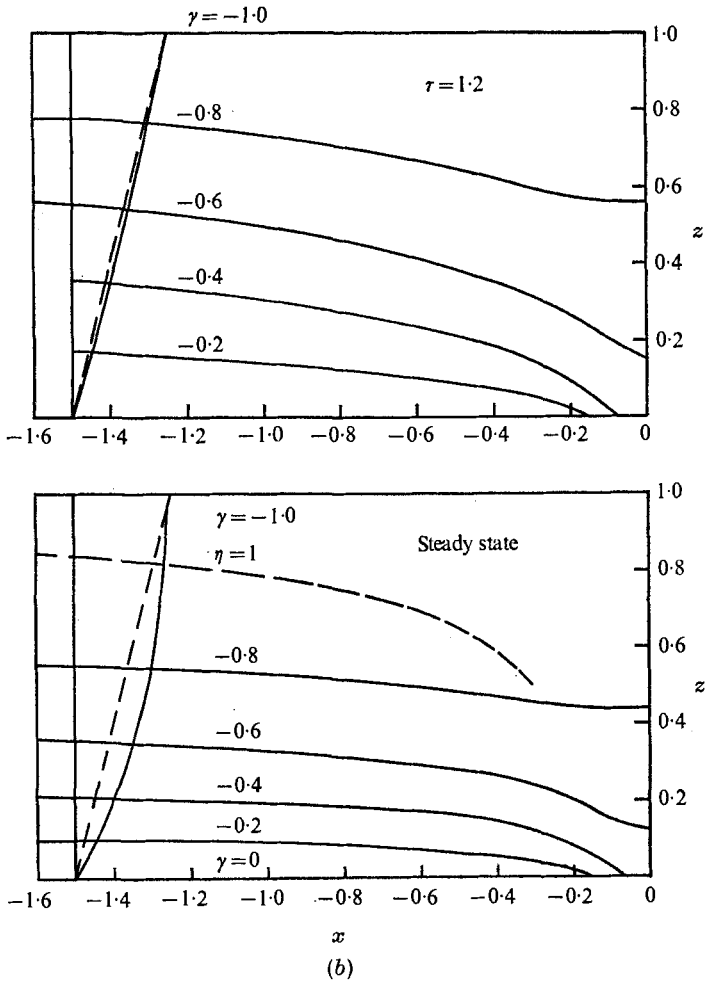

FIGURE 15. (*a*) Streamlines and (*b*) constant-density lines, for $F = 0{\cdot}20$, $Re = 10^6$, $Sc = 833$.

The flow in the upper right corner is seen to slow down substantially, and even to become almost stagnant, but no corner eddy appears. This is in contrast to Yih's solution for the same value of F. A reproduction of Yih's solution (Yih 1965, p. 85) is shown in figure 14(*b*), for comparison. Yih pointed out that the appearance of a slow corner eddy implies a breakdown of his solution; but the present numerical solution shows no such unrealistic feature. Indeed, in Yih's inviscid steady-state formulation, the solution does not exist for $F = \pi^{-1}$, implying perhaps some abrupt changes near $F = \pi^{-1}$; the numerical solution shows that the transition from non-selective to selective withdrawal is smooth. The critical value $F = \pi^{-1}$ only marks the division above which no waves can penetrate upstream, and hence no selective withdrawal. However, no abrupt changes in flow and density fields occur through this transition. For comparison, a steady-state flow pattern for $F = 0{\cdot}20$ is also shown in figure 15(*a*). It is seen that the transition from the supercritical to subcritical regime is indeed quite smooth. The transition

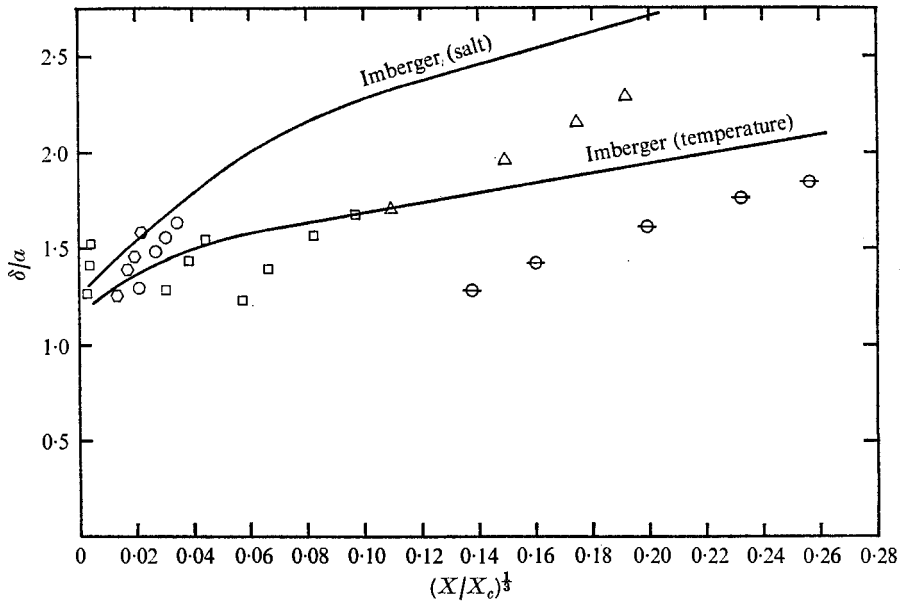

FIGURE 16. Numerical withdrawal-layer thickness as a function of $(X/X_c)^{\frac{1}{3}}$. ◇, $F = 0{\cdot}20$; □, 0·15; ○, 0·106. △, $F = 0{\cdot}032$, $Re = 40$, $Sc = 833$; ⊖, $F = 0{\cdot}106$, $Re = 100$, $Sc = 7{\cdot}14$.

is marked by the gradual appearance of stagnant zone in the top region as F decreases below π^{-1}. The thickness of the stagnant zone increases gradually instead of abruptly as F decreases through π^{-1}. The flow in the region above the line $\eta = 1$ is essentially stagnant (where $\eta = Zu_m^*/2Q$). Figure 15(*a*) also shows the flow pattern at an earlier time for $F = 0{\cdot}20$. Steepening of the streamlines and occurrence of a stagnant zone can be seen clearly. The constant-density lines are shown in figure 15(*b*).

The growth of the thickness of the withdrawal layer with distance from the sink is now obtained from the numerical solutions. This is shown in figure 16, in which δ/a is plotted against $(X/X_c)^{\frac{1}{3}}$, where $\delta = 2Q/u_m^*$, $a = (2Q/N)^{\frac{1}{2}}$ and $X_c = (2F)^{\frac{3}{2}}(\nu D)^{-\frac{1}{2}}Nd^3$ is a viscous–diffusive scale length, introduced by Imberger (1972). The two solid lines are the integral solution of Imberger† for salt and temperature. The points denote the present numerical solutions. From figure 16, we may discern two regimes of flow, inviscid and viscous, according to the magnitude of (X/X_c). For $(X/X_c)^{\frac{1}{3}}$ very small, say less than 0·05, X_c is no longer the appropriate scaling length. This is clearly seen, for example, in the case of $F = 0{\cdot}15$, figure 16, where δ/a is calculated at the same x but different X_c's. The values of δ/a for the same x remain unchanged, and do not depend on X_c for $(X/X_c)^{\frac{1}{3}} < 0{\cdot}05$. The solution is therefore inviscid, and is not scaled by X_c. For $(X/X_c)^{\frac{1}{3}} > 0{\cdot}05$, viscous and diffusive effects come into play. X_c is now an appropriate scaling length. The trend indicates an approach to Imberger's (1972) result. For that regime, it is also shown in the figure that the effect of diffusion, indicated by two different values of Sc corresponding to salt and tem-

† Although Imberger used the withdrawal thickness δ_{12}, which is defined to be the width at which the velocity has dropped to $\frac{1}{12}u_m$, no such distinction is made in figure 16.

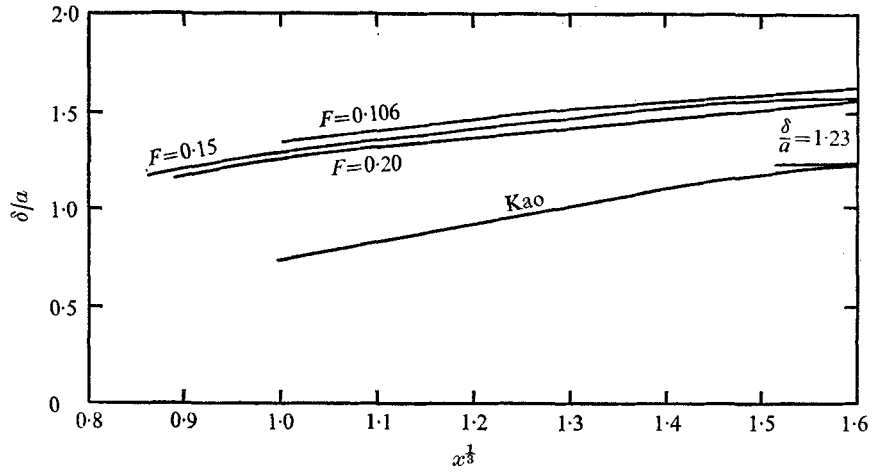

FIGURE 17. Numerical withdrawal-layer thickness as a function of $x^{\frac{1}{3}}$. $F = 0{\cdot}106$, $x_c = 1{\cdot}00 \times 10^5$; $F = 0{\cdot}15$, $x_c = 3{\cdot}46 \times 10^4$ and $x_c = 3{\cdot}16 \times 10^6$; $F = 0{\cdot}20$, $x_c = 3{\cdot}99 \times 10^5$.

perature, separates the solution into two distinct branches, again in agreement with Imberger's results. It is seen that the numerical curves are below those of Imberger. It will further be shown in part 2 that the present result is in better agreement with experiment. But it should be pointed out that, for $(X/X_c)^{\frac{1}{3}} < 1$, Imberger's result depends on the choice of a constant (K_3 in Imberger 1972). A certain degree of variation is thus allowed in Imberger's curves, depending on the matching condition to the inviscid region near the sink. Imberger applied the matching at $(X/X_c) = 0$, whereas it is seen that the matching should be done away from $(X/X_c) = 0$. In any case, the present results give the correct solution to the inviscid problem, and for small values of $(X/X_c)^{\frac{1}{3}}$.

Returning now to the inviscid regime, for which $(X/X_c)^{\frac{1}{3}} < 0{\cdot}05$, we find that a more appropriate plot would be δ/a against $x^{\frac{1}{3}}$. This is figure 17, which shows that δ/a is a function of $x^{\frac{1}{3}}$ only, and does not depend on X_c. In other words, for very small values of (X/X_c), the solution is indeed inviscid. That this is so also follows from Imberger's (1972) scaling arguments. The growth of δ/a with x is now due to the near-field effect of the sink. This point is brought out more clearly by comparing with Kao's (1970) inviscid free-streamline solution, which is also plotted in the figure. It is seen that the near-field growth of that solution for $1 < |x| < 4$ also follows $x^{\frac{1}{3}}$ to a good degree of approximation. For $|x| > 4$, no further growth is indicated.

The steady-state velocity profiles for $|x| < 4$ were computed from the numerical solution for $F = 0{\cdot}32$, $0{\cdot}20$, $0{\cdot}15$, $0{\cdot}106$, $0{\cdot}0713$ and $0{\cdot}032$. We now plot all the numerical values of u/u_m against the variable η. This is done in figure 18, which shows that the numerical points for all the computations with Froude numbers between $0{\cdot}032$ and $0{\cdot}20$ essentially collapse into a single curve. For comparison, the forward-moving portion of Koh's (1966*a*) solution for the linearized viscous–diffusive case, and the nonlinear large-Reynolds-number integral solution given by Imberger (1972) are also shown in the figure. In the present numeri-

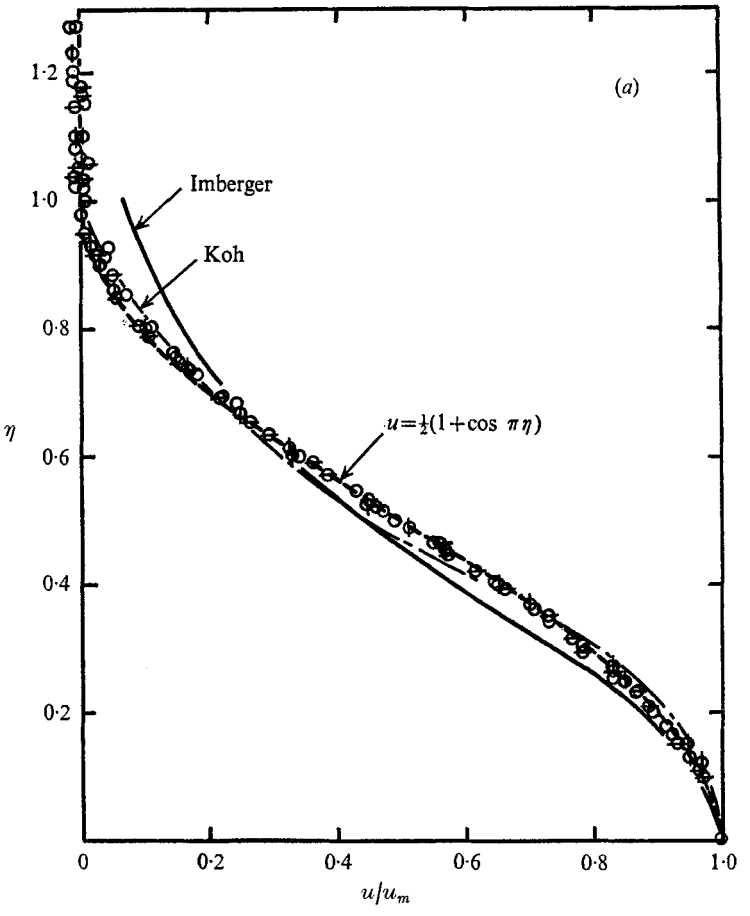

FIGURE 18(a). For legend see facing page.

cal computations, Re ranges from 20 to 10^6. It appears that there is overall agreement, in the similarity profile, between the present numerical results and previous results based on the boundary-layer assumption. On the other hand, provided that $Re > 10^4$, $Sc > 1$ and $(X/X_c)^{\frac{1}{3}} \ll 1$, the present results indicate that the steady state is established in an inviscid manner. This fact can be reconciled with Imberger's boundary-layer assumption, by observing that, while the velocity profile retains its boundary-layer nature, the scaling is no longer viscous–diffusive. The hydrostatic condition, which remains valid under the boundary-layer assumption in the limit of vanishing viscosity, is perhaps the more fundamental feature underlining the similarity. The present solution therefore settles, at least from a numerical viewpoint, the nature of the steady solution in the near field or for $(X/X_c) \ll 1$. It turns out that the similarity profile also fits very well the simple expression

$$\left.\begin{aligned} u/u_m &= \tfrac{1}{2}(1+\cos\pi\eta), \quad |\eta| \leqslant 1, \\ u/u_m &= 0, \qquad\qquad\quad |\eta| \geqslant 1. \end{aligned}\right\} \tag{34}$$

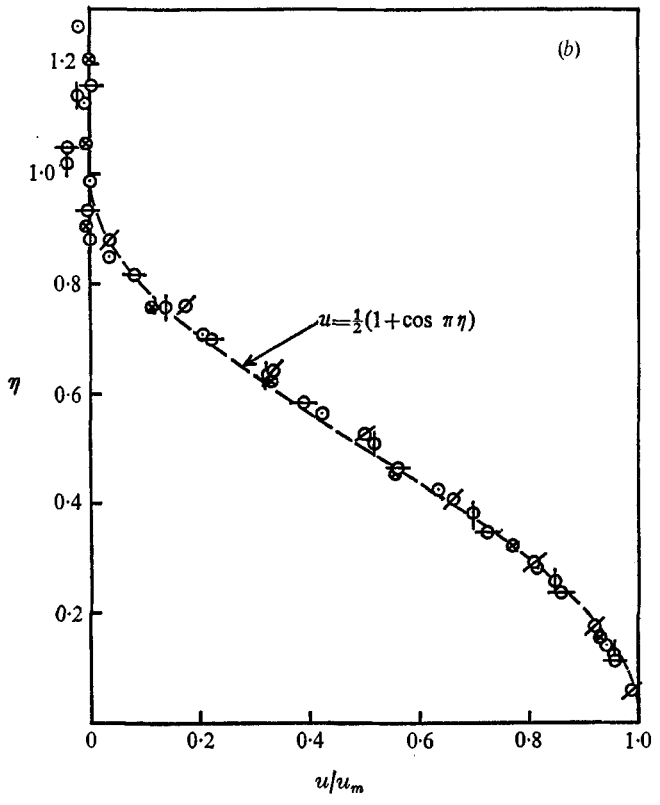

FIGURE 18. Steady-state horizontal velocity profiles at various F compared with Imberger's (——) and Koh's (— · —) result.

		F	Re	Sc
(*a*)	○	0·032	40	833
	Φ	0·106	100	7·14
	⊖	0·15	100	1000
(*b*)		0·15	10000	10

(*b*) ⊗, $x = -0{\cdot}640$; ⊙, $-0{\cdot}992$; Φ, $-1{\cdot}928$; ⊖, $-3{\cdot}081$; ∅, $-4{\cdot}105$.

In fact, figure 18 shows that (34) fits the numerical points better than Koh's and Imberger's theory. Moreover, the velocity profile in (34) satisfies the integral condition derived from the continuity equation; and it meets the η axis tangentially at $|\eta| = 1$. The value of Z at which $|\eta| = 1$ obviously delineates very well the thickness δ of the withdrawal layer (i.e. $\delta = 2Q/u_m^*$). This similarity profile will be discussed again in the light of our experimental data in part 2.

Since u_m is a function of x only, it can be shown, from (34) and the continuity equation, that the vertical velocity field is

$$\left.\begin{aligned} w &= -(u_m'/u_m)\eta(1+\cos\pi\eta), && |\eta| \leqslant 1,\\ w &= 0, && |\eta| \geqslant 1, \end{aligned}\right\} \tag{35}$$

where $u_m' = du_m/dx$.

The steady-state density fields for $|x| < 4$ were also computed for F ranging from 0·32 to 0·032. Density profiles at $x = -3$ for various F ranging from 0·20

F		0·32	0·20	0·15	0·15	0·106	0·106	0·0713	0·032	0·014	0·004
Re		10000	10^6	10000	100	3440	100	2255	40	625	20
Sc		1000	833	10	1000	1000	7·14	833	833	1000	7·14
x	−1·0	−2·7	−3·0	−2·9	−2·8	−2·8	−2·5	−2·8	−2·7	−2·5†	−1·9†
	−2·0	−1·8	−2·6	−2·6	−2·4	−2·5	−2·1	−2·5	−2·3	−2·2†	−1·7†
	−3·0	−1·4	−2·5	−2·3	−2·2	−2·3	−1·9	−2·3	−2·0	−2·0†	−1·6†

† These values are estimated from the time-dependent trend of the numerical solution.

TABLE 3. Numerical values of the density gradient at the centre-line $(\partial\gamma/\partial z)_{z=0}$

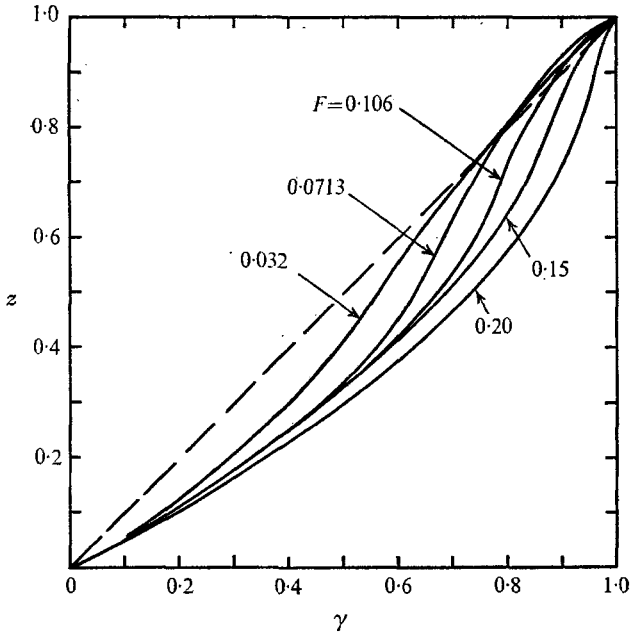

FIGURE 19. Steady-state density profiles at $x = -3$ for $F = 0{\cdot}032$, 0·0713, 0·106, 0·15 and 0·20.

to 0·032 are plotted in figure 19. It is seen that, for $z < 0{\cdot}4$, the density profiles are essentially the same for $0{\cdot}0713 < F < 0{\cdot}20$. Moreover, the density gradient at the centre-line increases substantially from the original value. Some numerical values of the density gradient at the centre-line are also given in table 3. It is seen that the density gradient at the centre-line, for large Re, is essentially independent of F for $0{\cdot}0713 < F < 0{\cdot}20$. For smaller values of F, the density gradient at the centre-line can still be estimated from the time-dependent trend of the numerical solution. This is also shown in table 3. The density gradient at the centre-line decreases as F decreases to small values. For the development of the flow discussed, the vertical convergence of the flow field in the vicinity of the centre-line is induced as columnar disturbances progress upstream; this in turn leads to increase of the density gradient there, since the density is essentially a conserved quantity here. (An analogous phenomenon also occurs in selective withdrawal in a rotating fluid (Pao & Shih 1973), where the radial convergence of the flow field, induced by the 'blocking waves', leads to the spin-up of the central core.)

The authors are indebted to the Atmospheric Sciences Section of the National Science Foundation for support under grant GA-23784.

REFERENCES

DEBLER, W. E. 1959 Stratified flow into a line sink. *J. Eng. Mech. Div., Proc. A.S.C.E.* **85**, 51–65.

IMBERGER, J. 1972 Two-dimensional sink flow of a stratified fluid contained in a duct. *J. Fluid Mech.* **53**, 329–349.

KAO, T. W. 1965 A free-streamline solution for stratified flow into a line sink. *J. Fluid Mech.* **21**, 535–543.

KAO, T. W. 1970 Free-streamline theory for inviscid stratified flow into a line sink. *Phys. Fluids*, **13**, 558–564.

KAO, T. W., PAO, H.-P. & WEI, S. N. 1972 Time dependent behaviour of stratified flow in a channel towards a line sink. *Int. Symp. Stratified Flow, IAHR*, Novosibirsk.

KAO, T. W., PAO, H.-P. & WEI, S. N. 1974 Dynamics of establishment of selective withdrawal from a line sink. Part 2. Experiment. *J. Fluid Mech.* **65**, 689.

KOH, R. C. Y. 1966*a* Viscous stratified flow towards a sink. *J. Fluid Mech.* **24**, 555–575.

KOH, R. C. Y. 1966*b* Unsteady stratified flow into a sink. *J. Hydraulic Res.* **4**, 21–35.

PAO, H.-P. & KAO, T. W. 1969 Sources and sinks at the axis of a viscous rotating fluid. *Phys. Fluids*, **12**, 1536–1546.

PAO, H.-P. & SHIH, H. H. 1973 Selective withdrawal and blocking wave in rotating fluids. *J. Fluid Mech.* **54**, 459–480.

SHIH, H. H. & PAO, H.-P. 1971 Selective withdrawal in rotating fluids. *J. Fluid Mech.* **49**, 409–527.

TORRANCE, K. E., & ROCKETT, J. A. 1969 Numerical study of natural convection in an enclosure with localized heating from below: creeping flow to the onset of laminar instability. *J. Fluid Mech.* **36**, 33–54.

TRUSTRUM, K. 1964 Rotating and stratified fluid flow. *J. Fluid Mech.* **19**, 415–432.

WUNDERLICH, W. O. 1971 The dynamics of density-stratified reservoirs. *American Fisheries Soc. Special Publication on Reservoirs.*

WUNDERLICH, W. O. & ELDER, R. A. 1968 Evaluation of Fontana Reservoir field measurements. *A.S.C.E. Speciality Conf. Current Res. into Effects of Reservoirs on Water Quality*, Portland, Oregon.

WUNDERLICH, W. O. & ELDER, R. A. 1971 Mechanics of flow through man-made lakes. *Symp. on Man-made Lakes, their Problems and Environmental Effects*, Knoxville, Tennessee.

YIH, C.-S. 1958 On the flow of a stratified fluid. *Proc. 3rd U.S. Nat. Cong. Appl. Mech.*, pp. 857–861.

YIH, C.-S. 1965 *Dynamics of Nonhomogeneous Fluids.* Macmillan.